A&A 603, A132 (2017)
DOI: 10.1051/0004-6361/201628792

Astronomy & Astrophysics

Millimeter observations of the disk around GW Orionis

M. Fang[1,2], A. Sicilia-Aguilar[3,1,4], D. Wilner[5], Y. Wang[6,7], V. Roccatagliata[8], D. Fedele[9], and J. Z. Wang[10]

[1] Departamento de Física Teórica, Universidad Autónoma de Madrid, 28049 Cantoblanco, Madrid, Spain
e-mail: mfang.cn@gmail.com
[2] Department of Astronomy, University of Arizona, 933 North Cherry Avenue, Tucson, AZ 85721, USA
[3] SUPA, School of Physics and Astronomy, University of St Andrews, North Haugh, St Andrews KY16 9SS, UK
[4] School of Science and Engineering, University of Dundee, Nethergate, Dundee DD1 4HN, UK
[5] Harvard-Smithsonian Center for Astrophysics, 60 Garden Street, Cambridge, MA 02138, USA
[6] Max Planck Institute for Astronomy, Königstuhl 17, 69117 Heidelberg, Germany
[7] Purple Mountain Observatory and Key Laboratory of Radio Astronomy, Chinese Academy of Sciences, 2 West Beijing Road, 210008 Nanjing, PR China
[8] Universitäts-Sternwarte München, Ludwig-Maximilians-Universität, Scheinerstr. 1, 81679 München, Germany
[9] INAF-Osservatorio Astrofisico di Arcetri, L.go E. Fermi 5, 50125 Firenze, Italy
[10] Shanghai Astronomical Observatory, Chinese Academy of Sciences, 80 Nandan Road, 200030 Shanghai, PR China

Received 25 April 2016 / Accepted 4 May 2017

ABSTRACT

The GW Ori system is a pre-main sequence triple system (GW Ori A/B/C) with companions (GW Ori B/C) at ∼1 AU and ∼8 AU, respectively, from the primary (GW Ori A). The primary of the system has a mass of 3.9 $M_{\odot}$, but shows a spectral type of G8. Thus, GW Ori A could be a precursor of a B star, but it is still at an earlier evolutionary stage than Herbig Be stars. GW Ori provides an ideal target for experiments and observations (being a "blown-up" solar system with a very massive sun and at least two upscaled planets). We present the first spatially resolved millimeter interferometric observations of the disk around the triple pre-main sequence system GW Ori, obtained with the Submillimeter Array, both in continuum and in the ^{12}CO $J = 2-1$, ^{13}CO $J = 2-1$, and C^{18}O $J = 2-1$ lines. These new data reveal a huge, massive, and bright disk in the GW Ori system. The dust continuum emission suggests a disk radius of around 400 AU, but the ^{12}CO $J = 2-1$ emission shows a much more extended disk with a size around 1300 AU. Owing to the spatial resolution (∼1″), we cannot detect the gap in the disk that is inferred from spectral energy distribution (SED) modeling. We characterize the dust and gas properties in the disk by comparing the observations with the predictions from the disk models with various parameters calculated with a Monte Carlo radiative transfer code RADMC–3D. The disk mass is around 0.12 $M_{\odot}$, and the disk inclination with respect to the line of sight is around ∼35°. The kinematics in the disk traced by the CO line emission strongly suggest that the circumstellar material in the disk is in Keplerian rotation around GW Ori. Tentatively substantial C^{18}O depletion in gas phase is required to explain the characteristics of the line emission from the disk.

Key words. circumstellar matter – stars: pre-main sequence – binaries: spectroscopic – stars: individual: GW Orionis

1. Introduction

Spectroscopic and imaging surveys suggest that a majority of young stars are formed in binary/multiple systems (Ghez et al. 1993; Leinert et al. 1993; Ghez et al. 1997; Lafrenière et al. 2008; Kraus et al. 2011). Theoretical and observational studies indicate that the interaction between disks and companions is an efficient mechanism for dissipating disks (Lin & Papaloizou 1993; Cieza et al. 2009; Kraus et al. 2012). Thus, it is very important to investigate disks around the binary or multiple stellar systems in order to understand disk evolution, as well as planet formation. The triple system GW Ori is an ideal target for such a study.

GW Ori is located at λ Ori (∼400 pc, Bell et al. 2013), and was recently revealed as a triple stellar system (GW Ori A/B/C, Mathieu et al. 1991; Berger et al. 2011). The primary GW Ori A is a G8 pre-main sequence star with a mass of ∼4 $M_{\odot}$, which makes it a very interesting system between Herbig Be stars and classical T Tauri stars (Fang et al. 2014). The close companion GW Ori B was discovered as a spectroscopic binary with an orbital period of ∼242 days and a separation of ∼1 AU (Mathieu et al. 1991; Fang et al. 2014). The second companion GW Ori C, located at a projected separation of ∼8 AU from GW Ori A, was detected with a near-infrared interferometric technique (Berger et al. 2011). The sub-millimeter and millimeter observations show that GW Ori is still harboring a massive disk (Mathieu et al. 1995), which is one of the most massive disks around a G-type star. Strong ongoing accretion activity ($\dot{M}_{\rm acc}$∼3–4 × 10^{-7} $M_{\odot}$ yr^{-1}) from the disk to the central star(s) in the GW Ori system has been suggested from the U-band excess, and strong and broad Hα and Hβ emission lines on the spectrum of GW Ori (Calvet et al. 2004; Fang et al. 2014).

In Fang et al. (2014, hereafter Paper I), we presented a study of the inner disk in the GW Ori system based on the infrared data. We reproduced the spectral energy distribution (SED) of GW Ori using disk models with gaps sized 25–55 AU. We found that the SED of GW Ori exhibited dramatic changes on timescales of ∼20 yr in the near-infrared bands, which can be interpreted as the change in the amount and distribution of dust particles in the gap due to a leaky dust filter. Because of its brightness at submillimeter and millimeter wavelengths, there has been much speculation regarding the system's disk mass and size; a radius of up to 500 AU and masses that could render it gravitationally unstable have been suggested (Mathieu et al. 1995; Schegerer et al. 2009). In this work, we present an investigation of the outer disk around GW Ori using the new millimeter data obtained from the

Submillimeter Array (SMA, Ho et al. 2004). These new observations have spatially resolved the disk around GW Ori for the first time. The paper is organized as follows. In Sect. 2 we describe the observations and data reduction. In Sect. 3 we present our observational results. In Sect. 4 we describe the disk modeling, and compare the model results with the observations, which are then discussed in Sect. 5. We summarize our results in Sect. 6.

2. Observations and data reduction

The object GW Ori was observed with the SMA on January 5, 2010, in the compact configuration with six antennas; on January 19, 2011, in the very extended configuration with six antennas; and on February 2, 2011, in the extended configuration with seven antennas. The phase center of the field was RA = $05^h29^m08.38^s$ and Dec = $+11°52'12.7''$ (J2000.0). The SMA has two spectral sidebands, both 4 GHz wide and separated by 10 GHz. The receivers were tuned to 230.538 GHz in the upper sideband (v_{lsr} = 11 km s^{-1}) with a maximum spectral resolution of 1.1 km s^{-1} on the upper sideband and 1.2 km s^{-1} on the lower sideband. The system temperatures (T_{sys}) were around ~80–200 K during the observation on January 5, 2010; ~100−200 K on January 19, 2011; and ~110−300 K on February 2, 2011. For the compact configuration on January 5, 2010, the bandpass was derived from the quasar 3c273 observations. Phase and amplitude were calibrated with regularly interleaved observations of the quasar 0530+135 (1.7° away from the source). The flux calibration was derived from Titan observations, and the flux scale is estimated to be accurate within 20%. For the very extended configuration on January 19, 2011, the bandpass was derived from the quasar 3c279 observations. Phase and amplitude were calibrated with regularly interleaved observations of the quasar 0530+135 and 0423−013. The flux calibration was derived from Ganymede observations, and the flux scale is estimated to be accurate within 20%. For the extended configuration on February 2, 2011, the bandpass was derived from the quasar 3c279 observations. Phase and amplitude were calibrated with regularly interleaved observations of the quasar 0530+135 and 0423−013. The flux calibration was derived from Titan observations, and the flux scale is estimated to be accurate within 20%.

We merged the three configuration data sets, applied different robust parameters for the continuum and line data, and obtained the synthesized beam sizes 1.03″ × 0.70″ (PA ~ 89.5°) and 1.15″ × 0.83″ (PA ~ −88.6°), respectively. The rms of 1.3 mm continuum image is 0.96 mJy beam^{-1}, and the rms of the ^{12}CO J = 2−1 data is 0.05 Jy beam^{-1} at 1.1 km s^{-1} spectral resolution, 0.04 Jy beam^{-1} at 1.2 km s^{-1} spectral resolution for ^{13}CO J = 2−1, and 0.03 Jy beam^{-1} at 1.2 km s^{-1} spectral resolution for C^{18}O J = 2−1. The flagging and calibration was done with MIR (Scoville et al. 1993), which was originally developed for the Owens Valley Radio Observatory and adapted for the SMA[1]. The imaging and data analysis were conducted in MIRIAD (Sault et al. 1995).

3. Observational results

3.1. Dust continuum emission

In Fig. 1a, we show the continuum emission map of GW Ori with contours starting at 4.8 mJy beam^{-1} (5σ) and increasing at 9.5mJy beam^{-1} (10σ) intervals. Considering a 20% systematic calibration uncertainty, the integrated continuum flux density in this map is 320 ± 64 mJy, consistent with the result (255 ± 60 mJy) in Mathieu et al. (1995). From a two-dimensional Gaussian fit to the image, the full width at half maximum (FWHM) of the continuum emission is 1.″4(±0.″004) × 1.″3(±0.″004), suggesting that the continuum emission of GW Ori is resolved given the synthesized beam size of 1.03″ × 0.70″. After the deconvolution of the synthesized beam, the FWHM of the continuum emission map is 0.″9 × 1.″1 which corresponds to 360 × 400 AU at a distance 400 pc. In Figs. 1c, d we show the distribution of the intensities for the continuum emission map along the east-west and north-south directions across the center of the map, and the expected distributions for an unresolved object according to the spatial resolutions of our observations. We note that the emission of GW Ori along the east-west direction is marginally resolved, but the emission along the north-south direction is well resolved.

3.2. Molecular line emission

In the top three panels in Fig. 2 we show the integrated intensity maps of the ^{12}CO J = 2−1, ^{13}CO J = 2−1, and C^{18}O J = 2−1 lines. The ^{12}CO J = 2−1 line emission map shows an elongated structure extended from the north-east to the south-west direction with a single peak coincided with the center of the continuum emission. The ^{12}CO J = 2−1 line emission map is clearly spatially resolved. A two-dimensional Gaussian fit to the ^{12}CO J = 2−1 integrated intensity map gives an FWHM size of 2.″5 × 3.″4 after the deconvolution of the synthesized beam, corresponding to 890 × 1300 AU at a distance 400 pc, which is much more extended than the continuum emission map. The ^{13}CO J = 2−1 line integrated intensity map of GW Ori is more compact than that for ^{12}CO J = 2−1, and comparable to the continuum emission map. From the disk of GW Ori, we only marginally detect the C^{18}O J = 2−1 line.

In Figs. 3a and 4a, we show the ^{12}CO J = 2−1 and ^{13}CO J = 2−1 velocity (first) moment maps, suggesting the northern and southern parts of the disk are redshifted and blueshifted with respect to the relative velocity of GW Ori, respectively. Figure 5 displays the channel maps of the ^{12}CO J = 2−1 line emission with contours starting at 0.127 Jy beam^{-1} (3σ) with intervals of 0.127 Jy beam^{-1}. The velocity moment maps and the channel maps are generally consistent with the expected kinematic pattern for gas material in Keplerian rotation with substantial inclination to our line of sight. The disk inclination can be constrained using the position-velocity (PV) diagram of the molecular lines. In Fig. 6a, we present the PV diagram from the ^{12}CO J = 2−1 map along the north-south direction across the peak of the integrated intensity maps of ^{12}CO J = 2−1. In the figure, we plot the expected Keplerian rotation curves for a disk inclined by 20°, 40°, and 60° around a star with a mass of 3.9 $M_\odot$ for comparison. From the comparison, we infer that the disk inclination should be between 20° and 60°.

Figure 5 shows the channel maps of ^{12}CO J = 2−1 line emission. In the figure, at the channels with velocities of 12.0 and 13.1 km s^{-1}, we note a tail structure originating from the outer disk and pointing to the north-western direction. A similar tail is also evident as the blueshifted structure in the ^{12}CO J = 2−1 velocity moment map. One explanation for the structure could be the cloud contamination, which can be severe for CO lines. If this is the case, the velocity of the parent cloud around GW Ori must be ~1 km s^{-1} bluer than GW Ori. A Gaussian fit to the ^{12}CO J = 2−1 spectrum at the peak of the integrated line intensity map suggests that the velocity of GW Ori with respect to the

[1] The MIR cookbook by Chunhua Qi can be found at http://cfa-www.harvard.edu/~cqi/mircook.html

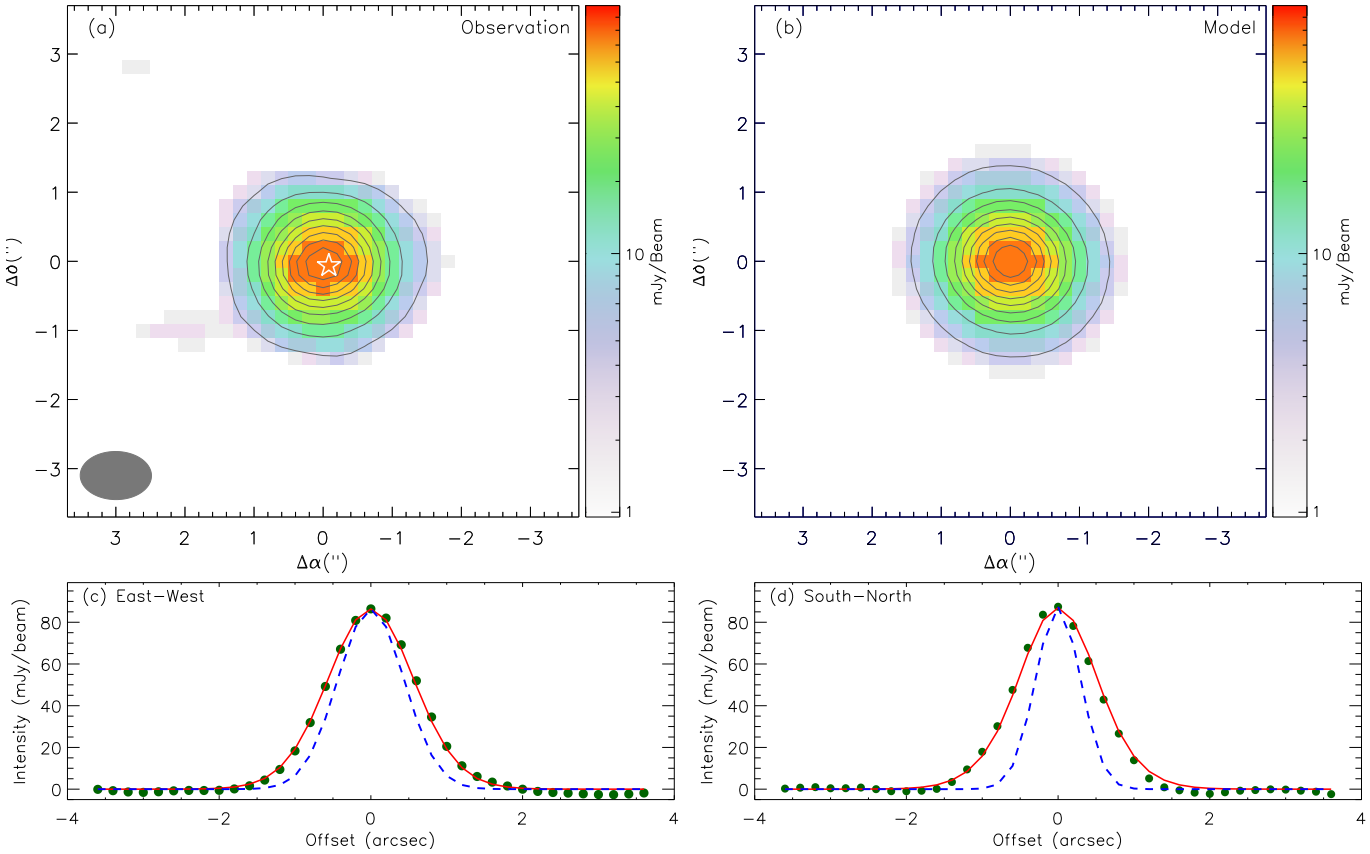

Fig. 1. a) Observed map of the continuum emission observed toward GW Ori at a wavelength of 1.3 mm, with contours (solid lines) drawn at 9.5 mJy beam^{-1} (10σ) intervals, starting at 4.8 mJy beam^{-1} (5σ). The synthesized beam is shown in the lower left corner. The position of the central star is indicated with the star symbol. **b)** Modeled map of the continuum emission for the GW Ori disk system at a wavelength of 1.3 mm. The contour levels are the same as in panel **a)**. **c), d)** Distribution of the observed intensities (filled circles) along the east-west **c)** and north-south **d)** directions across the center of the map compared with the our model (solid lines). The dashed lines show the expected profiles for an unresolved object.

local standard of rest (LSR) is around 13.6 km s^{-1}, and the LSR velocity of the parent cloud of GW Ori is around 12.7 km s^{-1} (Lang et al. 2000), which supports the above explanation of the blueshifted tail structure.

4. Disk modeling

In this section, we use a simple disk model to reproduce the SMA observations of GW Ori. Our data has low spatial resolution, which means that any model using these data involves a strong simplification of the very complex GW Ori disk system (Fang et al. 2014). Furthermore, the complexity of disks means that the parameter space is highly degenerated and non-continuous (Sicilia-Aguilar et al. 2016). Our aim is thus to explore the global gas and dust content of the GW Ori disk in the light of typical disk models and to compare these values to those of other similar objects. Any further modeling is beyond the scope of this paper and will be worthwhile only when higher resolution data becomes available.

4.1. Continuum emission

4.1.1. Parameters for modeling continuum emission

We define a global dust surface density in the same form as in Andrews et al. (2009),

$$\Sigma = \Sigma_c \left(\frac{R}{R_c}\right)^{-\gamma} \exp\left[-\left(\frac{R}{R_c}\right)^{2-\gamma}\right], \quad (1)$$

where Σ_c is the normalization parameter at the characteristic scaling radius R_c, and γ is the gradient parameter. The above profile, which has been used to successfully model different types of disks in the literature (Andrews et al. 2009, 2011, 2012), is the similarity solution for a simple accretion disk with time-independent viscosity (ν) and $\nu \propto R^\gamma$ (Lynden-Bell & Pringle 1974; Hartmann et al. 1998). In this work, we do not take Σ_c as the free parameter. Instead, we use the disk dust mass ($M_{\rm dust}$), and Σ_c can be calculated when we set up other parameters describing the disk structure. We set γ as a free parameter.

We include a vertical gradient in the dust size distribution in the disk model to simulate the dust settling in disks. In practice, we use two dust populations: a small dust population and a large dust population, as did Andrews et al. (2011). The dust density structure for each dust population in a spherical coordinate system (R, θ, and ϕ) is parameterized as

$$\rho_{\rm small} = \frac{(1-f)\Sigma}{\sqrt{2\pi}Rh} \exp\left[-\frac{1}{2}\left(\frac{\pi/2-\theta}{h}\right)^2\right], \quad (2)$$

$$\rho_{\rm large} = \frac{f\Sigma}{\sqrt{2\pi}R\Lambda h} \exp\left[-\frac{1}{2}\left(\frac{\pi/2-\theta}{\Lambda h}\right)^2\right], \quad (3)$$

where $\rho_{\rm small}$ is the density for the small dust population, $\rho_{\rm large}$ the density for the large dust population, and h the angular scale height. Following Andrews et al. (2011), we assume the large grains are distributed to 20% of the scale height ($\Lambda = 0.2$), and account for 85% of the total column ($f = 0.85$). We do not explore the parameter space of Λ and f since our observational

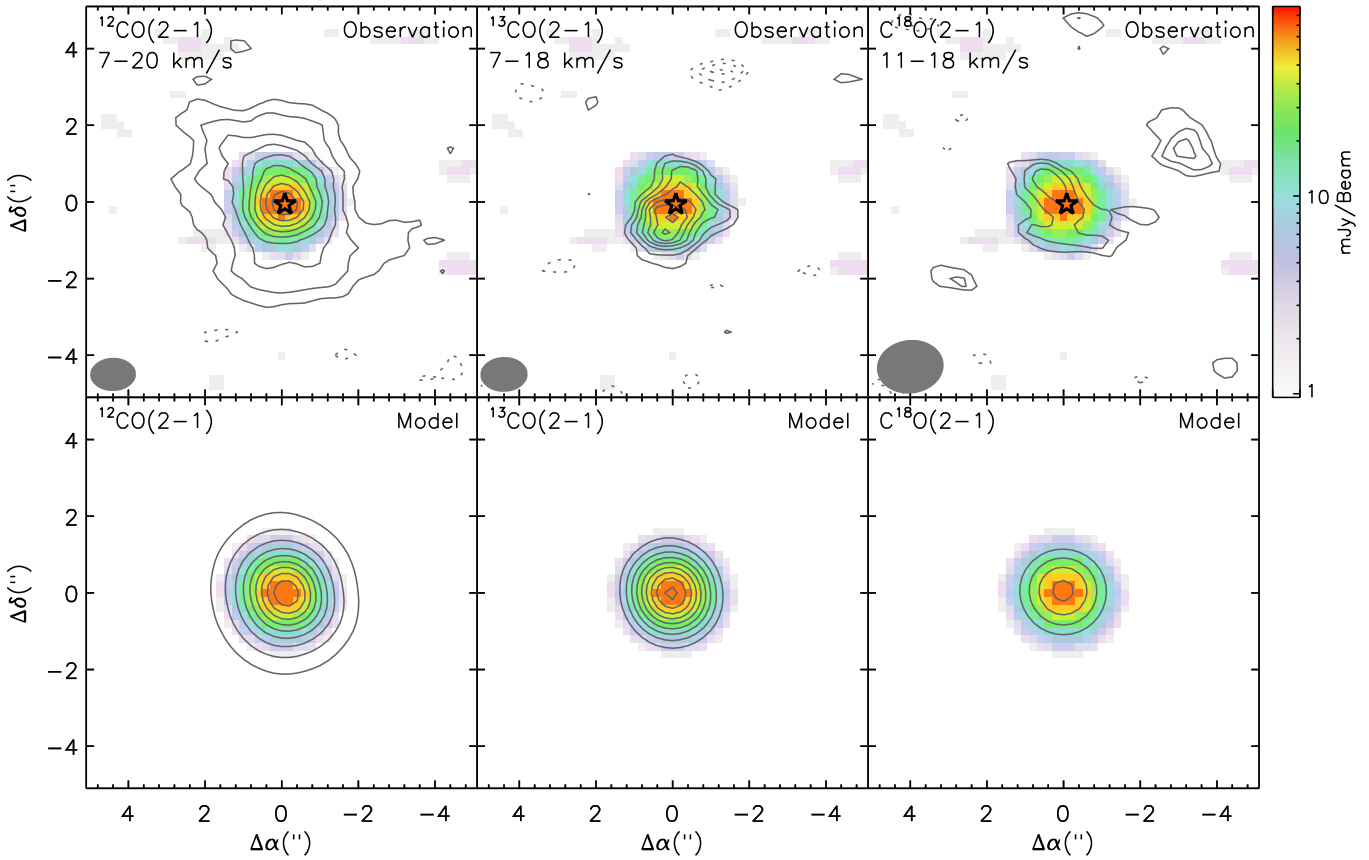

Fig. 2. *Top panels*: velocity-integrated intensities (contours) for the ^{12}CO J = 2–1, ^{13}CO J = 2–1, and C^{18}O J = 2–1 line emission, overlaid on the continuum emission. For ^{12}CO J = 2–1, the intensities are integrated over the velocity range between 6.5 and 20.8 km s^{-1}; the contours are drawn at 0.69 Jy beam^{-1} km s^{-1} (3σ) intervals, starting at 0.69 Jy beam^{-1} km s^{-1} (3σ). For ^{13}CO J = 2–1, the intensities are integrated over the velocity range between 7 and 20 km s^{-1}; the contours start at 0.48 Jy beam^{-1} km s^{-1} (3σ) with an interval of 0.16 Jy beam^{-1} km s^{-1} (1σ). For C^{18}O J = 2–1, the intensities are integrated over the velocity range between 7 and 20 km s^{-1}; the contours begin at 0.24 Jy beam^{-1} km s^{-1} (3σ) and increase in 0.08 Jy beam^{-1} km s^{-1} (1σ) increments. In each panel, the negative contours (dashed lines) are drawn at −1σ intervals, starting at −3σ. The synthesized beam for each line emission is shown in the lower left corner in each panel. *Bottom panels*: modeled velocity-integrated intensities (contours) for the ^{12}CO J = 2–1, ^{13}CO J = 2–1, and C^{18}O J = 2–1 line emission, overlaid on the modeled continuum emission for the GW Ori disk system. The contour levels are the same as in the *top panels* at the corresponding molecular lines.

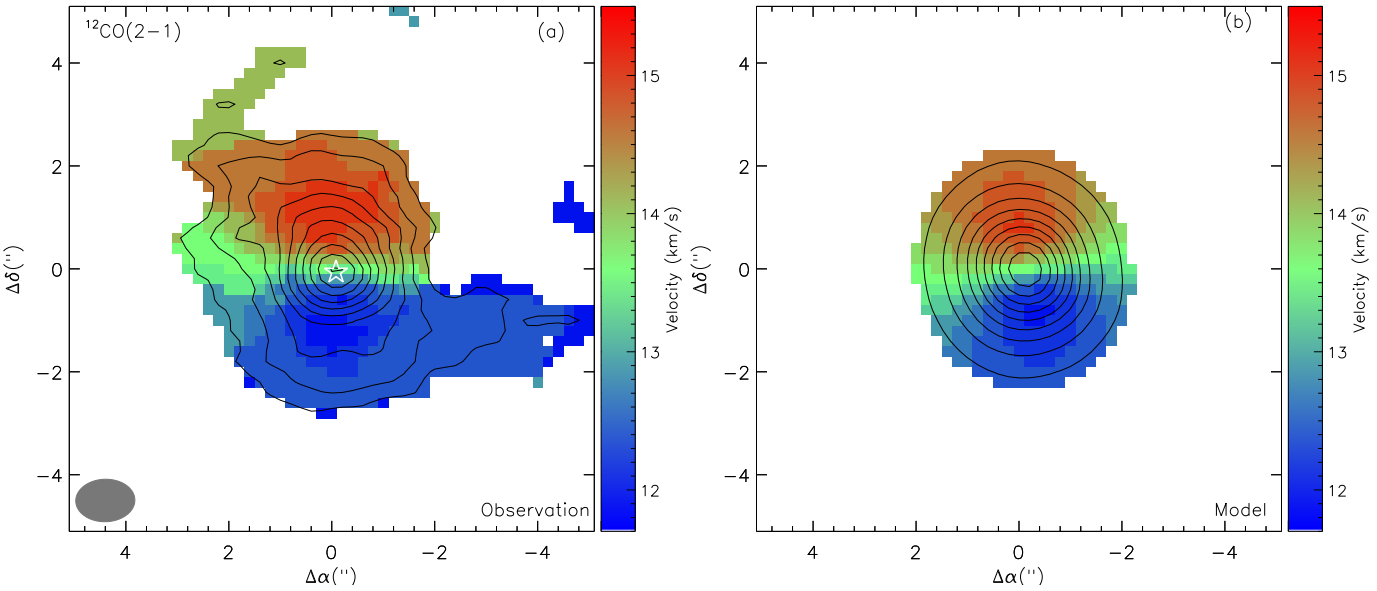

Fig. 3. a) ^{12}CO J = 2–1 velocity (first) moment map. The contours are for the ^{12}CO J = 2–1 velocity-integrated intensities (see Fig. 2), starting at 0.69 Jy beam^{-1} km s^{-1} (3σ) with an interval of 0.69 Jy beam^{-1} km s^{-1} (3σ). The synthesized beam is shown in the lower left corner. **b)** Same as in panel **a)**, but for the predicted map from modeling.

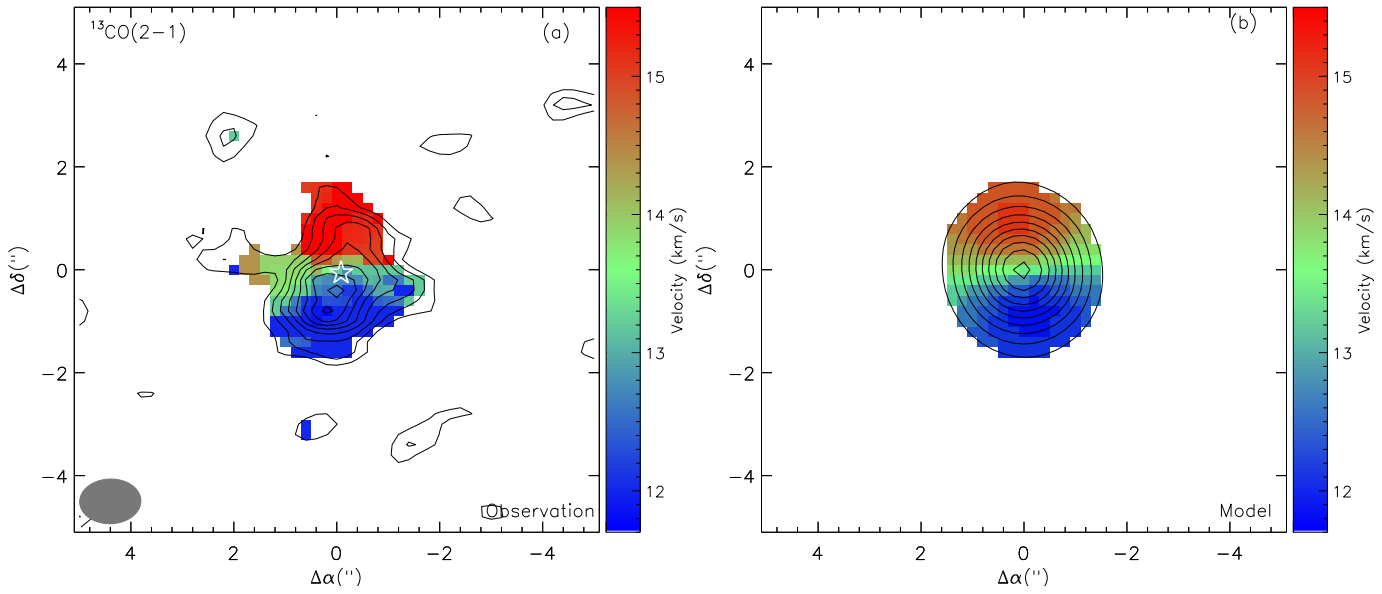

Fig. 4. a) ^{13}CO $J = 2-1$ velocity (first) moment maps. The contours are for the ^{13}CO $J = 2-1$ velocity-integrated intensities (see Fig. 2), starting at 0.48 Jy beam^{-1} km s^{-1} (3σ) with an interval of 0.16 Jy beam^{-1} km s^{-1} (1σ). The synthesized beam is shown in the lower left corner. **b)** Same as in panel **a)**, but for the predicted map from modeling.

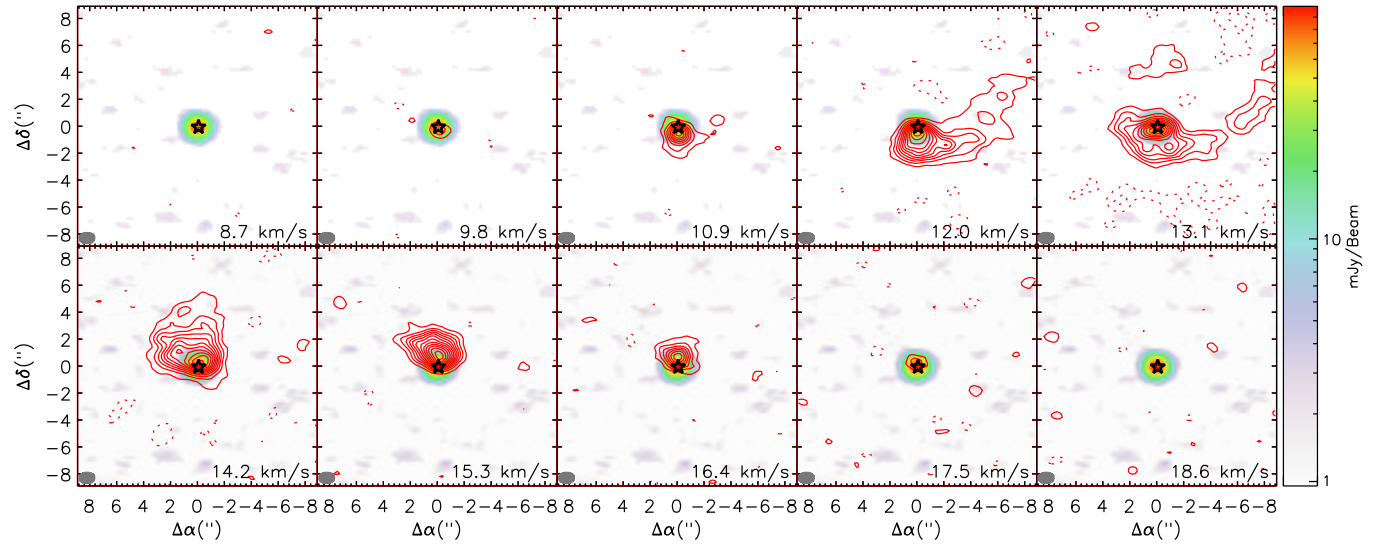

Fig. 5. Channel maps of the ^{12}CO $J = 2-1$ emission toward GW Ori. Channels are 1.1 km s^{-1} wide with the synthesized beam marked in the bottom left corner. Contour levels are drawn at intervals of 0.127 Jy beam^{-1} (3σ), starting at 0.127 Jy beam^{-1}. The dashed contours are the negative features with the same contours as the positive ones in each panel. The synthesized beam is shown in the lower left corner in each panel.

data cannot provide an efficient constraint on them. The angular scale height h is defined as

$$h = h_{\rm c}\left(\frac{R}{R_{\rm c}}\right)^{\Psi}, \quad (4)$$

where $h_{\rm c}$ is the angular scale height at the scaling radius $R_{\rm c}$, and Ψ characterizes the flaring angle of the disk.

In Paper I, we have shown that a gap sized at 25–55 AU needs to be included in the disk model. A small population of tiny dust particles (sizes 0.005–1 μm) should also be distributed throughout the gap in order to reproduce the moderate excess emission at near-infrared bands and the strong and sharp silicate feature at 10 μm on the SED of GW Ori. In this work, we include a dust depletion factor ($\xi_{\rm gap}$) to modify the surface density within the gap. We simply set the gap size $R_{\rm gap} = 45$ AU, according to the results in Paper I, since our SMA data cannot provide any constraints on the inner disk. The inner radius of the gap ($R_{\rm in}$) is fixed at 1.2 AU, which is the orbital semi-major axis of the close companion GW Ori B (see Paper I). When the disk radius $R \le R_{\rm gap}$, the modified surface density is $\Sigma = \xi_{\rm gap}\Sigma$, where Σ is obtained from Eq. (1).

In the disk models, we use two populations of amorphous dust grains (25% carbon and 75% silicate) with a power-law size distribution with an exponent of −3.5 and a minimum size of 0.005 μm. The maximum size of dust grains is set at 1 μm in the gap, as suggested in Paper I, and at 1 μm for the small dust population and 1000 μm for the large dust population in the outer disk ($R > R_{\rm gap}$). In Fig. 7, we show the opacity spectra for the two dust populations derived from Mie calculations.

The stellar parameters adopted in the models are $T_{\rm eff} = 5500$ K, $R_\star = 7.6\,R_\odot$, and $M_\star = 3.9\,M_\odot$, taken from Paper I. We use the RADMC–3D code (version 0.40, Dullemond 2012)

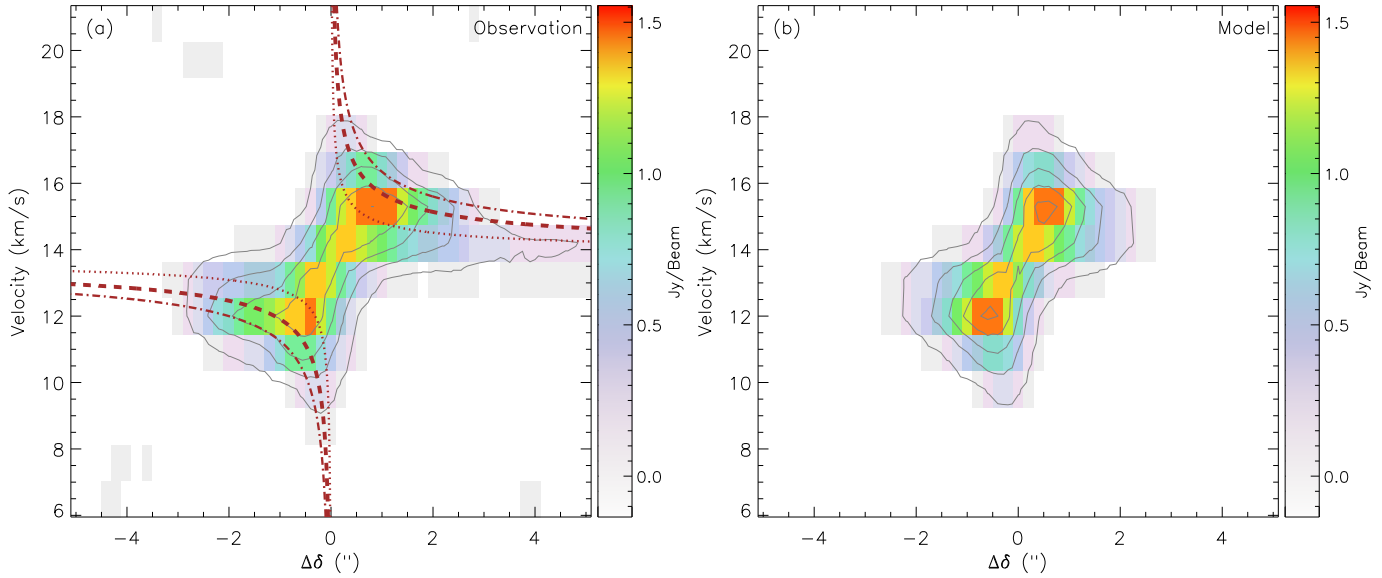

Fig. 6. a) Observed position-velocity diagram from the ^{12}CO $J = 2-1$ map along the north-south direction across GW Ori. The offset refers to the distance along the cut from GW Ori. The contours start at 0.15 Jy beam^{-1} (3σ) with an interval of 0.05 Jy beam^{-1} (1σ). The dotted, dashed, and dash-dotted lines show a Keplerian rotation curve with a central mass of 3.9 $M_\odot$ with disk inclinations of 20°, 40°, and 60°, respectively. **b)** Same as in panel **a)**, but for the modeled position-velocity diagram with a disk inclination of 35°.

to perform the radiative transfer calculations in the disk models, and vary the free parameters to calculate the continuum emission maps at 1.3 mm and the SEDs. For simplicty, we convolve the model continuum emission maps with the synthetical beam for the SMA continuum emission map to simulate the observations.

4.1.2. Scheme for modeling continuum emission

In order to model the continuum emission from the disk of GW Ori, we have ten parameters. Eight of these parameters, $R_{\rm in}$, $R_{\rm gap}$, $\xi_{\rm gap}$, $R_{\rm c}$, γ, $h_{\rm c}$, Ψ, and $M_{\rm dust}$, are for the disk structure. As discussed above, we have fixed $R_{\rm in} = 1.2$ AU, $R_{\rm gap} = 45$ AU. To compare the model results with the observations, we need to know the orientation of the disk with respect to the observer; this can be characterized with two more parameters, the inclination (i) of the disk with respect to the line of sight ($i = 90°$ for edge-on disks) and the position angle (PA) of the disk major axis. The disk of GW Ori is well resolved in the ^{12}CO $J = 2-1$ line. From the integrated intensity map of the ^{12}CO $J = 2-1$ line, we derive an inclination of ~40° and a position angle of ~10°. When modeling the disk, we allow the inclination to vary (30°, 40°, and 50°) and fix the position angle at 10°.

The exploration of the parameter spaces is divided into three steps. At the first step, we calculate the continuum emission map at 1.3 mm for a coarse and wide grid of parameters listed in Table 1. Here we fix $\xi_{\rm gap} = 3 \times 10^{-3}$, according to the SED modeling in Paper I, since it only insignificantly affects the 1.3 mm continuum emission modeling. In total, we obtain 9360 modeled 1.3 mm continuum emission maps. We compare the calculated continuum emission maps with the observation, which can efficiently constrain $M_{\rm dust}$ and $R_{\rm c}$. For each model, the goodness of the fit $\chi^2_{\rm mm}$ is calculated by

$$\chi^2_{\rm mm} = \frac{\frac{1}{N}\sum_{i=1}^{N}(\mu_i - \omega_i)^2}{\sigma^2}, \quad (5)$$

where σ is the noise of the observed 1.3 mm map, N the number of pixels with values above 3σ, μ the modeled data, and ω the observed data. By comparing these data with the observations, we obtain sets of disk models providing a good fit that we define as $\chi^2_{\rm mm} - \chi^2_{\rm mm,\,best} < 2$, where $\chi^2_{\rm mm,\,best}$ is the minimum $\chi^2_{\rm mm}$ of all the models. In total, we have 102 good-fit models. Then, we calculate the SEDs of the good-fit disk models in the range from 70 μm to 1.3 mm, and compare them with that of GW Ori. The goodness of the fit of the SED $\chi^2_{\rm SED}$ is calculated by

$$\chi^2_{\rm SED} = \frac{1}{N}\sum_{i=1}^{N}\frac{(\mu_i - \omega_i)^2}{\sigma_i^2}, \quad (6)$$

where N is the number of the observed wavelengths, μ the synthetic flux density, ω the observed flux density, and σ the observational uncertainities. The total goodness of the fit $\chi^2_{\rm total}$ is given by

$$\chi^2_{\rm total} = \chi^2_{\rm mm} + \chi^2_{\rm SED}. \quad (7)$$

We derive the ranges for the free parameters of the models providing a good fit with $\chi^2_{\rm total} - \chi^2_{\rm total,\,best} < 2$, where $\chi^2_{\rm total,\,best}$ is the minimum $\chi^2_{\rm total}$ of the 102 models. The parameters of the good-fit models are listed in Table 1.

At the second step, we refine the grid of parameters with knowledge of the above good-fit models, and list them in Table 2. We repeat the procedure in the first step, but require $\chi^2_{\rm mm} - \chi^2_{\rm mm,\,best} < 0.5$ and $\chi^2_{\rm total} - \chi^2_{\rm total,\,best} < 0.5$. We obtain the ranges for the free parameters of the models providing a fit with $\chi^2_{\rm total} - \chi^2_{\rm total,\,best} < 0.5$. The disk model with minimum $\chi^2_{\rm total}$ is considered to be the best-fit model.

At the final step, we constrain the dust depletion factor ($\xi_{\rm gap}$) by fitting the full SED of GW Ori. We calculate a set of model SEDs by varing $\xi_{\rm gap}$ from 1×10^{-3} to 1×10^{-2} with other parameters from the above best-fit model. Since the change of $\xi_{\rm gap}$ can only vary the shape of the SED within near- and mid-infrared wavelengths, we compare the model SEDs with the observed one within the wavelengths ranging from 1 μm to 37 μm. We find the model SEDs with $\xi_{\rm gap} = 1.5-4 \times 10^{-3}$ can reproduce the observations, and the one with $\xi_{\rm gap} = 2.5 \times 10^{-3}$ can give the best

Table 1. Coarse grids of the parameters for modeling disk continuum emission.

Parameters	Input	Range ($\chi^2_{\rm total} - \chi^2_{\rm total,\ best} < 2$)
	Central star	
Effective temperature ($T_{\rm eff}$)[a]	5500 K	
Stellar radius[a]	7.5 $R_\odot$	
Stellar mass ($M_\star$)[a]	3.9 $M_\odot$	
	Disk	
Inner radius ($R_{\rm in}$)[a]	1.2 AU	
Gap size ($R_{\rm gap}$)[a]	45 AU	
Dust depletion factor ($\xi_{\rm gap}$)[a]	3×10^{-3}	
Characteristic scaling radius ($R_{\rm c}$)	250, 270, 290, 310, 330, 350, 370, 390 AU	290–350 AU
Surface density gradient parameter (γ)	0.1, 0.3, 0.5, 0.7, 0.9, 1.1	0.1–0.5
Angular scale height ($h_{\rm c}$)	0.15,0.17,0.19,0.21,0.23	0.15–0.19
Ψ	0.1, 0.15, 0.2	0.1–0.2
Disk mass	[1, 1.5, 2, 2.5, 3, 3.5, 4, 4.5, 5, 5.5, 6, 6.7, 7] $\times 10^{-2}\ M_\star$	3–3.5 $\times 10^{-2}\ M_\star$
Disk inclination (i)	30°, 40°, 50°	30°–40°
Position angle[a]	10°	

Notes. [(a)] Fixed parameters.

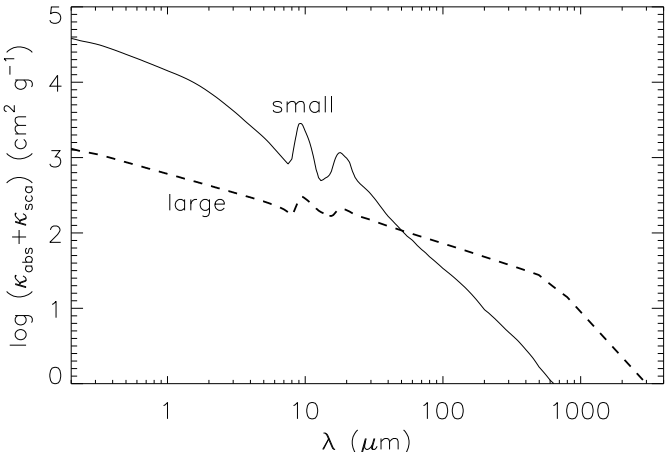

Fig. 7. Opacity spectra ($\kappa_{\rm abs}$ for absorption and $\kappa_{\rm sca}$ for scattering) for the small dust population (solid line) and the large dust population (dash line) used in our disk modeling.

fit to the data. As mentioned before, our model is highly simplified and the low resolution does not allow us to explore in depth the degenerated and non-continuous parameter space of this very complex system. Thus, the χ^2 approach should be taken as a tool to measure the goodness of fit, but it cannot be used to derive statistics on the significance of any particular model.

4.2. CO emission

With the parameters of the above best-fit model, we can compute the model map of the ^{12}CO $J = 2-1$ velocity-integrated intensities and compare it with the observation. However, to calculate the CO emission, we need to know the gas temperature distribution in the disk. At the first step, we assume that the gas and dust have equal temperatures, and ignore that CO molecules are frozen out of the gas phase when $T_{\rm gas} < 20$ K and that the gas temperatures may be higher than the dust temperatures near the disk surface. The velocity fields of gas material in the disk models are assumed to be Keplerian. The thermal line broadening is automatically included in the RADMC–3D code. In addition, we also include the turbulent line broadening by assuming a constant line width of 0.01 km s^{-1} from turbulence. Taking an abundance ratio ^{12}CO/H$_2$ = 10^{-4}, which is the canonical abundance of the interstellar medium (ISM), we calculate the ^{12}CO $J = 2-1$ line emission using the RADMC–3D code with an assumption of local thermal equilibrium (LTE) conditions. The resulting maps are simply convolved with the corresponding synthetical beams, and then compared with the observation. We find that the predicted peak intensity of ^{12}CO $J = 2-1$ is about 3 times weaker than the observation. We vary the parameters among the good-fit models listed in Table 2, and the model emission for the ^{12}CO $J = 2-1$ line are all 2–3 times weaker than the observation. The previous studies have shown that the gas temperatures could exceed the dust temperatures in the disk surface layers (Qi et al. 2006; Panić et al. 2009), possibly due to additional ultraviolet or X-ray heating from central stars (Glassgold et al. 2004; Jonkheid et al. 2004). In order to reproduce the observed CO emissions of GW Ori, following Andrews et al. (2012), we parameterize the gas temperature as

$$T_{\rm gas} = \begin{cases} T_{\rm atm} + (T_{\rm mid} - T_{\rm atm}) \left[\cos\left(\frac{\pi}{2}\frac{\pi/2-\theta}{h_{\rm q}}\right)\right]^{2\delta} & \text{if } \pi/2 - \theta < h_q \\ T_{\rm atm} & \text{if } \pi/2 - \theta \geq h_q. \end{cases} \quad (8)$$

Here $T_{\rm mid}$ is the midplane temperature derived from the RADMC–3D simulations of the dust, δ describes the steepness of the vertical profile, and $h_{\rm q} = 4H_{\rm p}$, where $H_{\rm p}$ is the angular pressure scale height determined from $T_{\rm mid}$. We calculate $H_{\rm p}$ as $H_{\rm p} = (kT_{\rm mid}R/GM_\star\mu m_{\rm H})^{1/2}$, where k is the Bolzmann constant, G is the gravitational constant, $\mu = 2.37$ is the mean molecular weight of the gas, and $T_{\rm atm}$ is the temperature in the disk atmosphere, parameterized as

$$T_{\rm atm} = T_{\rm atm,100\,AU}\left(\frac{R}{100\,{\rm AU}}\right)^{\zeta}. \quad (9)$$

For gas temperatures, we only set $T_{\rm atm,100\,AU}$ as a free parameter and fix $\delta = 2$ and $\zeta = -0.5$. We assume that the CO molecules

Table 2. Refined grids of the parameters for modeling disk continuum emission.

Parameters	Input	Range ($\chi^2_{\rm total} - \chi^2_{\rm total,\ best} < 0.5$)	Best-fit
Characteristic scaling radius (R_c)	290, 300, 310, 320, 330, 340, 350 AU	300–340 AU	320 AU
Surface density gradient parameter (γ)	0.1, 0.2, 0.3, 0.4, 0.5	0.1–0.4	0.2
Angular scale height (h_c)	0.15, 0.16, 0.17, 0.18, 0.19	0.15–0.19	0.18
Ψ	0.1, 0.15, 0.2	0.1-0.2	0.1
Disk mass	$[3.0, 3.1, 3.2, 3.3, 3.4, 3.5] \times 10^{-2}\ M_\star$	$3.0–3.4 \times 10^{-2}\ M_\star$	$3.1 \times 10^{-2}\ M_\star$
Disk inclination (i)	30°, 35°, 40°	30°–35°	35°

are frozen out of the gas phase when $T_{\rm gas} < 20$ K. Since ^{12}CO $J = 2–1$ line emission can be used to constrain the disk inclination better than dust continuum emission, we calculate the ^{12}CO $J = 2–1$ line emission using three disk inclinations, 30°, 35°, and 40°. The ^{12}CO $J = 2–1$ line emission values are computed using RADMC-3d assuming non-local thermal equilibrium (non-LTE) conditions for different $T_{\rm atm,100\,AU}$. The result integrated intensity maps of ^{12}CO $J = 2–1$ are simply convolved with the corresponding synthetical beams, and then compared with the observations to characterize $T_{\rm atm,100\,AU}$. For each model, the goodness of the fit $\chi^2_{\rm CO}$ is calculated in the same way as Eq. (5), but only for the pixels with values above half of the peak intensity to reduce the possibility of CO contamination by the parent cloud. We also compare the PV diagrams from the observation and from the models to constrain the disk inclination. From a χ^2 test, we find that a disk model with $T_{\rm atm,100\,AU} = 200 \pm 10$ K and $i = 35°–40°$ can fit the observations. In Table 3, we list the best-fit parameter for modeling the continuum and gas emission of GW Ori.

4.3. Model results

In our disk models, we have eight free parameters. The dust depletion factor ($\xi_{\rm gap}$) is mainly constrained by comparing the model SEDs with the observed values at near- and mid-infrared wavelengths, h_c can be estimated by fitting the SED at mid- and far-infrared bands, and $M_{\rm dust}$ can be constrained by fitting the SED of GW Ori at submillimeter and millimeter wavelengths and the 1.3 mm continnum emission map. The parameters R_c and γ are mainly constrained by comparing the model continuum emission map at 1.3 mm with the observations. The disk inclination (i) is constrained by fitting the 1.3 mm continuum emission map, the ^{12}CO $J = 2–1$ line emission map, and the PV diagram. The gas temperature parameter $T_{\rm atm,100\,AU}$ is constrained by fitting the ^{12}CO $J = 2–1$ line emission map. In Table 3, we list the disk model that can satisfactorily reproduce both the 1.3 mm continnum emission, the SED, and the ^{12}CO $J = 2–1$ line emission of GW Ori. In the following, we compare the model results using these parameters with the observations.

In Fig. 1b, we show the model continuum emission at 1.3 mm. In Figs. 1c, d, we compare the distribution of the intensity along the east-west and north-south directions across the center of the map from the model. The model results can fit the observations well. In Fig. 8, we compare the model SED with the observed value. The observed SED in the figure is the type 1 SED for GW Ori in Paper I and is constructed using the $UBVR_CI_C$ photometry from Calvet et al. (2004); the JHK_s photometry from the 2MASS survey (Skrutskie et al. 2006); the photometry at 3.4, 4.6, 12, and 22 μm from the WISE survey (Wright et al. 2010); the photometry at 9 and 18 μm from the AKARI survey (Ishihara et al. 2010); the MIPS 70 μm photometry from Paper I; the fluxes at 350, 450, 800, 850, 1100, and 1360 μm from Mathieu et al. (1995); and the 5–37 μm low-resolution IRS spectrum from Paper I. In Fig. 8 it can be seen that our simple disk model can reproduce well the observed SED of GW Ori. In Fig. 2 we show the model map of the ^{12}CO $J = 2–1$ velocity-integrated intensities calculated with the parameters in Table 3, which reproduces the observation very well. Figure 3b displays the model ^{12}CO $J = 2–1$ velocity moment map, and Fig. 6b shows the model PV diagram for the ^{12}CO $J = 2–1$ lines[2].

Table 3. Disk model parameters for modeling dust and gas emission of GW Ori.

Parameters	Values
Central star	
Effective temperature[a]	5500 K
Stellar radius[a]	7.5 $R_\odot$
Stellar mass[a]	3.9 $M_\odot$
Disk	
Inner radius ($R_{\rm in}$)[a]	1.2 AU
Gap size ($R_{\rm gap}$)[a]	45 AU
Dust depletion factor ($\xi_{\rm gap}$)	2.5×10^{-3}
Characteristic scaling radius (R_c)	320 AU
Surface density gradient parameter (γ)	0.2
Angular scale height (h_c)	0.18
Ψ	0.1
Disk mass	0.12 $M_\odot$
$T_{\rm atm,100\,AU}$	200 K
Power index for $T_{\rm atm}$ (ζ)[a]	−0.5
δ[a]	2
Disk inclination (i)	35°
Position angle[a]	10°

Notes. [(a)] Fixed parameters.

Using the disk parameters listed in Table 3, and taking the typical abundances of ISM for ^{13}CO and C^{18}O, ^{13}CO/H$_2$ = 1.43×10^{-6} and C^{18}O/H$_2$ = 1.82×10^{-7}, i.e. ^{12}CO/^{13}CO = 70 and ^{12}CO/C^{18}O = 550 (Wilson & Rood 1994), we calculate the predicted emission of the ^{13}CO and C^{18}O lines using RADMC–3D assuming non-LTE conditions. We note that the predicted line emission of ^{13}CO $J = 2–1$ is consistent with the observations (see Figs. 2 and 4b), but the model line emission of C^{18}O $J = 2–1$ is three times stronger than the observational data. A simple solution to reduce the model line emission is to decrease the abundance of C^{18}O in gas phase, which can be due to the real reduction in their abundances or more freezing

[2] The LSR velocity of GW Ori is assumed to be 13.6 km s^{-1} (see Sect. 3.2).

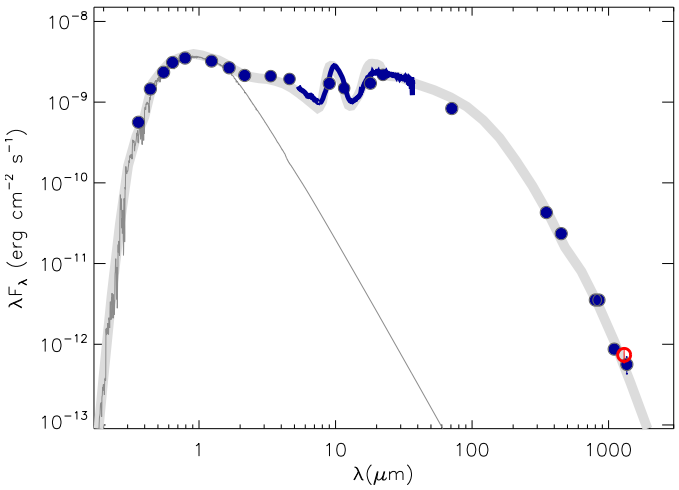

Fig. 8. Observed SED of GW Ori. The broadband photometry is shown with the filled circles, and the IRS spectrum of this source is indicated by a solid line. The open circle shows the flux from our SMA observations. The thick gray line shows our model SED. The photospheric emission level is indicated by a thin gray curve.

than we assumed. We find that a satisfactory fit to the SMA data requires that $C^{18}O/H_2 \sim 2.3 \times 10^{-8}$. In Fig. 2, we show the model map of $C^{18}O$ $J = 2-1$ velocity-integrated intensities calculated using the above abundances. A similar global $C^{18}O$ gas-phase depletion in circumstellar disks has been suggested before (Dutrey et al. 1994, 1996; Dartois et al. 2003; Isella et al. 2007), which can be due to a selective photodissociation of CO and its isotopes in disks (Visser et al. 2009). However, we must stress that the constraint on the abundance of $C^{18}O$ in the disk of GW Ori based on the SMA data is just tentative since the detection of $C^{18}O$ is marginal. Furthermore, an underestimate of the dust absorption of the line emission in the disk modeling or oversubtraction of continuum around $C^{18}O$ $J = 2-1$ could complicate the issue.

We have shown that our disk model can reproduce the SMA observations of GW Ori. However, multi-parameter disk models are known to be highly degenerated and non-continuous. In addition, there are other sources of uncertainty in disk modeling. The dust growth and settling in disks can change the dust properties vertically and radially (Birnstiel et al. 2010, 2012). In addition, it is unknown whether the gas and dust are well mixed in the GW Ori disk, and the gas-to-dust ratio may vary vertically and radially (Birnstiel et al. 2010). All these factors put strong limitations on the interpretations of the results from our disk modeling. The inferred disk masses can be strongly dependent on the assumed dust model (size distribution) and gas-to-dust ratio. In addition, it is expected that the structure of the disk, vertical scale height, dust distribution, and heating may differ from typical cases, due to the interaction between the two companions and the very massive disk in GW Ori.

5. Discussion

The disk inclination of GW Ori is constrained by the gas kinematics in the disk traced by the ^{12}CO line, which gives an intermediate inclination (~35°). In Paper I we estimated the inclination of the stellar rotation axis of the primary star (GW Ori A), which is around 35–50°. Thus, the stellar rotation axis of GW Ori A and the disk spin axis could be aligned. It is still unclear if the binary orbital plane and the disk is aligned in the GW Ori system. If it is the case, the mass of the close companion GW Ori B is estimated to be 0.44 $M_\odot$ using the minimum companion mass ($m_2 \sin i_* = 0.25$, i_* is the inclination of the orbit) derived in Paper I. In this case, the expected H-band flux ratio between the primary GW Ori A (3.9 $M_\odot$) and GW Ori B (0.44 $M_\odot$) is 30:1 at the age of ~0.9 Myr from the pre-main sequence evolutionary tracks of Siess et al. (2000). On the contrary, the near-infrared interferometric observations show that the two stellar components may have near-equal H-band fluxes (2:1), which requires a low inclination of the orbit (~10°) for GW Ori to have a massive close companion GW Ori B. However, an inclined orbit of a massive companion can drastically disturb the disk (Larwood et al. 1996). In addition, Shevchenko et al. (1998) detected the eclipses toward GW Ori during 1987–1992, which may suggest a nearly edge-on inclination of the orbit for GW Ori A/B. However, recent observation with *Kepler*/K2 observations detect many quasi-periodic or aperiodic dimming events from young stars with disks, which are not edge-on, and could be due to inclined and variable inner dust disk warps (Ansdell et al. 2016a,b; Scaringi et al. 2016). Thus, an intermediate disk inclination of GW Ori does not contradict the observation from Shevchenko et al. (1998).

6. Summary

Using the SMA we mapped the disk around GW Ori both in continuum and in the $J = 2-1$ transitions of ^{12}CO, ^{13}CO, and $C^{18}O$. The dust and gas properties in the disk are obtained by comparing the observations with the predictions from disk models with various parameters.

We find clear evidence that the circumstellar material in the disk is in Keplerian rotation around GW Ori with a disk inclination of ~35°.

We present a disk model that can reproduce the dust continuum and line emission of CO and its isotopes from the disk of GW Ori. To reproduce the line emission of $C^{18}O$, we may need the substantially depleted abundances of $C^{18}O$ in gas phase.

GW Ori is one of the most remarkable disks in terms of its mass, and one of the most remarkable stellar systems (a massive G8 star with two companions). This object is bright over the whole electromagnetic spectrum and well studied, and is an ideal target for future observations with ALMA.

Acknowledgements. M.F. acknowledges the support of the action "Proyectos de Investigación fundamental no orientada", grant number AYA2012-35008. A.S.A. acknowledges the support of the Spanish MICINN/MINECO "Ramón y Cajal" program, grant number RYC-2010-06164, and the action "Proyectos de Investigación fundamental no orientada", grant number AYA2012-35008. Y.W. acknowledges the support from NSFC through grants 11303097. D.F. acknowledges suppport from the Italian Ministry of Education, Universities and Research, project SIR (RBSI14ZRHR). This research has made use of the SIMBAD database, operated at CDS, Strasbourg, France. This publication makes use of data products from the Two Micron All Sky Survey, which is a joint project of the University of Massachusetts and the Infrared Processing and Analysis Center/California Institute of Technology, funded by the National Aeronautics and Space Administration and the National Science Foundation. This publication makes use of data products from the Wide-field Infrared Survey Explorer, which is a joint project of the University of California, Los Angeles, and the Jet Propulsion Laboratory/California Institute of Technology, funded by the National Aeronautics and Space Administration. This research is based on observations with AKARI, a JAXA project with the participation of ESA. This work is in part based on observations made with the *Spitzer* Space Telescope, which is operated by the Jet Propulsion Laboratory, California Institute of Technology under a contract with NASA.

References

Andrews, S. M., Wilner, D. J., Hughes, A. M., Qi, C., & Dullemond, C. P. 2009, ApJ, 700, 1502
Andrews, S. M., Wilner, D. J., Espaillat, C., et al. 2011, ApJ, 732, 42
Andrews, S. M., Wilner, D. J., Hughes, A. M., et al. 2012, ApJ, 744, 162
Ansdell, M., Gaidos, E., Rappaport, S. A., et al. 2016a, ApJ, 816, 69
Ansdell, M., Gaidos, E., Williams, J. P., et al. 2016b, MNRAS, 462, L101
Bell, C. P. M., Naylor, T., Mayne, N. J., Jeffries, R. D., & Littlefair, S. P. 2013, MNRAS, 434, 806
Berger, J.-P., Monnier, J. D., Millan-Gabet, R., et al. 2011, A&A, 529, L1
Birnstiel, T., Dullemond, C. P., & Brauer, F. 2010, A&A, 513, A79
Birnstiel, T., Klahr, H., & Ercolano, B. 2012, A&A, 539, A148
Calvet, N., Muzerolle, J., Briceño, C., et al. 2004, AJ, 128, 1294
Cieza, L. A., Padgett, D. L., Allen, L. E., et al. 2009, ApJ, 696, L84
Dartois, E., Dutrey, A., & Guilloteau, S. 2003, A&A, 399, 773
Dullemond, C. P., Juhasz, A., Pohl, A., et al. 2012, Astrophysics Source Code Library [record ascl: 1202.015]
Dutrey, A., Guilloteau, S., & Simon, M. 1994, A&A, 286, 149
Dutrey, A., Guilloteau, S., Duvert, G., et al. 1996, A&A, 309, 493
Fang, M., Sicilia-Aguilar, A., Roccatagliata, V., et al. 2014, A&A, 570, A118
Ghez, A. M., Neugebauer, G., & Matthews, K. 1993, AJ, 106, 2005
Ghez, A. M., McCarthy, D. W., Patience, J. L., & Beck, T. L. 1997, ApJ, 481, 378
Glassgold, A. E., Najita, J., & Igea, J. 2004, ApJ, 615, 972
Hartmann, L., Calvet, N., Gullbring, E., & D'Alessio, P. 1998, ApJ, 495, 385
Ho, P. T. P., Moran, J. M., & Lo, K. Y. 2004, ApJ, 616, L1
Isella, A., Testi, L., Natta, A., et al. 2007, A&A, 469, 213
Ishihara, D., Onaka, T., Kataza, H., et al. 2010, A&A, 514, A1
Jonkheid, B., Faas, F. G. A., van Zadelhoff, G.-J., & van Dishoeck, E. F. 2004, A&A, 428, 511
Kraus, A. L., Ireland, M. J., Martinache, F., & Hillenbrand, L. A. 2011, ApJ, 731, 8
Kraus, A. L., Ireland, M. J., Hillenbrand, L. A., & Martinache, F. 2012, ApJ, 745, 19
Lafrenière, D., Jayawardhana, R., Brandeker, A., Ahmic, M., & van Kerkwijk, M. H. 2008, ApJ, 683, 844
Lang, W. J., Masheder, M. R. W., Dame, T. M., & Thaddeus, P. 2000, A&A, 357, 1001
Larwood, J. D., Nelson, R. P., Papaloizou, J. C. B., & Terquem, C. 1996, MNRAS, 282, 597
Leinert, C., Zinnecker, H., Weitzel, N., et al. 1993, A&A, 278, 129
Lin, D. N. C., & Papaloizou, J. C. B. 1993, in Protostars and Planets III, eds. E. H. Levy, & J. I. Lunine, 749
Lynden-Bell, D., & Pringle, J. E. 1974, MNRAS, 168, 603
Mathieu, R. D., Adams, F. C., & Latham, D. W. 1991, AJ, 101, 2184
Mathieu, R. D., Adams, F. C., Fuller, G. A., et al. 1995, AJ, 109, 2655
Panić, O., Hogerheijde, M. R., Wilner, D., & Qi, C. 2009, A&A, 501, 269
Qi, C., Wilner, D. J., Calvet, N., et al. 2006, ApJ, 636, L157
Sault, R. J., Teuben, P. J., & Wright, M. C. H. 1995, in Astronomical Data Analysis Software and Systems IV, eds. R. A. Shaw, H. E. Payne, & J. J. E. Hayes, ASP Conf. Ser., 77, 433
Scaringi, S., Manara, C. F., Barenfeld, S. A., et al. 2016, MNRAS, 463, 2265
Schegerer, A. A., Wolf, S., Hummel, C. A., Quanz, S. P., & Richichi, A. 2009, A&A, 502, 367
Scoville, N. Z., Carlstrom, J. E., Chandler, C. J., et al. 1993, PASP, 105, 1482
Shevchenko, V. S., Grankin, K. N., Mel'Nikov, S. Y., & Lamzin, S. A. 1998, Astron. Lett., 24, 528
Sicilia-Aguilar, A., Banzatti, A., Carmona, A., et al. 2016, PASA, 33, e059
Siess, L., Dufour, E., & Forestini, M. 2000, A&A, 358, 593
Skrutskie, M. F., Cutri, R. M., Stiening, R., et al. 2006, AJ, 131, 1163
Visser, R., van Dishoeck, E. F., & Black, J. H. 2009, A&A, 503, 323
Wilson, T. L., & Rood, R. 1994, ARA&A, 32, 191
Wright, E. L., Eisenhardt, P. R. M., Mainzer, A. K., et al. 2010, AJ, 140, 1868